

# Fracturing in wet granular media illuminated by photoporomechanics

Yue Meng,<sup>1</sup> Wei Li,<sup>1</sup> and Ruben Juanes<sup>1,\*</sup>

<sup>1</sup>Massachusetts Institute of Technology,

77 Massachusetts Avenue, Cambridge, MA, USA

(Dated: November 30, 2022)

## Abstract

8 We study fluid-induced deformation and fracture of granular media, and apply photoporome-  
9 chanics to uncover the underpinning grain-scale mechanics. We fabricate spherical photoelastic  
10 particles of 2 mm diameter to form a monolayer granular pack in a circular Hele-Shaw cell that is  
11 initially filled with a viscous fluid. The key distinct feature of our system is that, with spherical par-  
12 ticles, the granular pack has a connected pore space, thus allowing for pore-pressure diffusion and  
13 the study of effective stress in coupled poromechanical processes. We inject air into the fluid-filled  
14 photoelastic granular pack, varying the initial packing density and confining weight. With our re-  
15 cently developed experimental technique, photoporomechanics, we find two different modes of fluid  
16 invasion: fracturing in fluid-filled elastic media (with strong photoelastic response), and viscous  
17 fingering in frictional fluids (with weak or negligible photoelastic response). We directly visualize  
18 the evolving effective stress field, and discover an effective stress shadow behind the propagating  
19 fracture tips, where the granular pack exhibits undrained behavior. We conceptualize the system's  
20 behavior by means of a mechanistic model for a wedge of the granular pack bounded by two grow-  
21 ing fractures. The model captures the pore pressure build-up inside the stress shadow region, and  
22 the grain compaction in the annular region outside. Our model reveals that a jamming transition  
23 determines the distinct rheological behavior of the wet granular pack, from a friction-dominated  
24 to an elasticity-dominated response.

## 25 INTRODUCTION

26 Multiphase flow through granular and porous materials exhibits complex behavior, the  
27 understanding of which is critical in many natural and industrial processes. Examples in-  
28 clude infiltration of water into the vadose zone [1], growth and deformation of cells and  
29 tissues [2], and geological carbon dioxide storage [3]. While fluid-fluid displacement in rigid  
30 porous media has been studied in depth, the understanding of the interplay between multi-  
31 phase flow and granular mechanics remains an ongoing challenge [4]. In many granular-fluid  
32 systems, the powerful coupling among viscous, capillary, and frictional forces leads to a  
33 wide range of patterns, including desiccation cracks [5, 6], fractures [7–13], labyrinth struc-  
34 tures [14], granular fingers [15–17], corals, and stick-slip bubbles [18]. An in-depth study  
35 of poromechanics behind these coupled solid-fluid processes is crucial to understanding a  
36 wide range of phenomena, including methane migration in lake sediments [19], shale gas  
37 production [20], and hillslope infiltration and erosion after forest fires [21].

38 While fracturing during gas invasion in fluid-saturated media has been studied extensively  
39 in experiments [7, 8, 10–13, 16, 22] and simulations [9, 17, 23–29], the underlying grain-scale  
40 mechanisms behind the morphodynamics and rheologies exhibited by deformable granu-  
41 lar media remain poorly understood. To investigate the interplay between fluid and solid  
42 mechanics of granular media, we adopt a recently developed experimental technique, *photo-*  
43 *toporomechanics* [30], to directly visualize the evolving effective stress field in a fluid-filled  
44 granular medium during the fracturing process. The key idea behind our photoporome-  
45 chanics technique is the manufacturing of residual-stress-free photoelastic particles (such as  
46 spheres or icosahedra) that allow for connectivity of the pore space, so that pore pressure  
47 can diffuse and one fluid can displace another even without grain motion. In an earlier study  
48 of root growth in photoelastic granular media, Barés et al. [31] manufactured cylindrical  
49 photoelastic particles with a groove on the edge to allow for roots to grow between adjacent  
50 grains and propagate deep inside the granular medium. This disc-with-groove geometry,  
51 however, would likely experience strong adhesion/friction with the walls of the Hele-Shaw  
52 cell, and it's a less realistic representation of granular materials than spherical particles.  
53 Given the importance of frictional forces on the morphological regimes of the granular pack  
54 [18, 22], here we focus on the impact of confining weight on the fracture patterns. We  
55 also adopt packing density as a control variable, which proves to be key to rheological and

56 morphological transitions in granular-fluid systems [18, 28].

57 In this study, we uncover two modes of air invasion under different initial packing den-  
58 sities and confining weights: fracturing in fluid-filled elastic media, and viscous fingering in  
59 frictional fluids. We discover an effective stress shadow behind the propagating fracture tips,  
60 where the intergranular stress is low and the granular pack exhibits undrained behavior. In  
61 the annular region outside the fractured region, the mechanical response of the granular  
62 medium transitions from friction-dominated to elasticity-dominated. To explain the ob-  
63 served distinct rheological behavior, we propose a mechanistic model for a wedge between  
64 two fractures. Finally, we rationalize the emergence of fracturing across our experiments as  
65 a jamming transition.

## 66 MATERIALS AND METHODS

67 Following the fabrication process in [30], we produce photoelastic spherical particles with  
68 a diameter  $d = 2$  mm (with 3.5% standard deviation) and a volumetric modulus  $K_p =$   
69 1.6 MPa. We inject air into a monolayer of photoelastic particles saturated with silicone oil  
70 ( $\eta = 9.71$  Pa·s) in a circular Hele-Shaw cell [Fig. 1]. When particles are immersed in silicone  
71 oil, the friction coefficient between particles is  $\mu_p = 0.2 \pm 0.06$ , and the friction coefficient  
72 between the particle and the glass plate is  $\mu_w = 0.05 \pm 0.02$ . To observe the photoelastic  
73 response of the particles, we construct a dark-field circular polariscope by means of a white  
74 light panel together with left and right circular polarizers [32]. Vertical confinement is  
75 supplied by a weight,  $W$ , adding up the weights from a confining weight, a light panel,  
76 a polarizer, and a glass disk that rests on top of the particles. The free top plate with  
77 prescribed confining weight is a natural representation of the conditions that prevail in  
78 subsurface processes, where the vertical confining stress is constant and controlled by the  
79 depth of the geologic stratum. To allow the fluids (but not the particles) to leave the cell,  
80 the disk is made slightly smaller than the interior of the cell (inner diameter  $L = 21.2$  cm),  
81 resulting in a thin gap around the edge of the cell. A coaxial needle is inserted at the  
82 center of the granular pack for saturation, fluid injection and pore pressure measurement.  
83 We conduct experiments in which we fix the air injection rate ( $q = 100$  mL/min) and the  
84 syringe reservoir volume ( $V_0 = 15$  mL). We use three linear variable differential transformers  
85 (LVDTs) to monitor the vertical displacement of the top plate. We adopt a dual-camera

86 system to record bright-field (camera A) and dark-field (camera B) videos. For the sample  
87 preparation, the initial packing density ( $\phi_0$ ) of the granular pack is controlled by the total  
88 mass of particles ( $M_s$ ), and is calculated in 2D through image analysis. Before the air  
89 injection, we take a bright-field photo of the granular pack and create a binary mask with  
90 an intensity threshold. We then calculate the initial 2D packing density ( $\phi_0$ ) by dividing  
91 the number of particle pixels by the total number of pixels in the circular Hele-Shaw cell.  
92 To study the impact of packing density and frictional force, we vary  $\phi_0$  from 0.78 to 0.84  
93 ( $M_s = 37$  to 40 g), and the confining weight  $W$  from 25 N to 85 N. The influence of the  
94 confining weight ( $W$ ) on  $\phi_0$  is negligible (< 0.2%).

95 To gain additional insight into the rheological behavior of the granular pack, we record  
96 the spatiotemporal evolution of the packing density and effective stress fields from the ex-  
97 periments. To construct the 2D packing density field, we create a binary mask, then detect  
98 particle positions by centroid finding in MATLAB, and compute the packing density at each  
99 particle position within a sampling radius  $3d$  [33] by dividing the number of particle pixels  
100 by the total number of pixels within the sampling circle. We then construct the packing  
101 density field for all the particles in the granular pack. To construct the effective stress  
102 field, we retrieve the light intensity of the blue channel from dark-field images and convert  
103 it into the effective stress value. To obtain the conversion factor between light intensity  
104 and effective stress, we conduct a single-bead calibration that directly relates light intensity  
105 to inter-particle force  $F$  [30]. By computing the Cauchy stress tensor for the calibrated  
106 particle under the diametrical loading condition, we obtain the expression that relates the  
107 inter-particle force to the effective stress,  $\sigma' = \frac{6F}{\pi d^2}$  [34]. After this conversion, we visualize  
108 the time evolution of the effective stress field from the dark-field images.

## 109 RESULTS AND DISCUSSION

110 In Fig. 2, we show the invasion patterns resulting from air injection for experimental  
111 conditions with the same confining weight ( $W = 25$  N) and two different initial packing  
112 fractions ( $\phi_0 = 0.84, 0.78$ ). The invasion patterns at breakthrough—when the invading fluid  
113 first reaches the outer boundary—indicate two invasion regimes: (I) fracturing in fluid-filled  
114 elastic media, with strong photoelastic response [Fig. 2(a)], and (II) viscous fingering in  
115 frictional fluids, with weak or negligible photoelastic response [Fig. 2(b)]. A light intensity

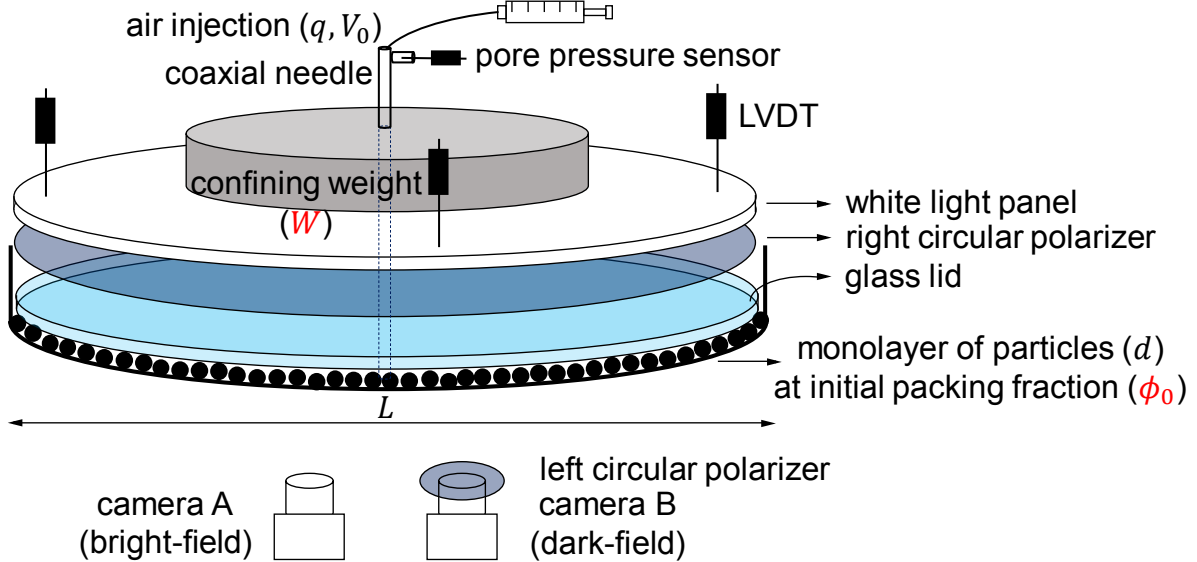


FIG. 1. Experimental setup: a monolayer of photoelastic particles (diameter  $d$ , initial packing density  $\phi_0$ ) saturated by silicone oil is confined in a circular Hele-Shaw cell (internal diameter  $L$ ). Vertical confinement is supplied by a weight,  $W$ , adding up the weights from a confining weight, a light panel, a polarizer, and a glass disk that rest on top of the particles. The disk is slightly smaller than the cell to allow the fluids (but not particles) to leave the cell. Air is injected at a fixed flow rate  $q$  at the center of the cell with a coaxial needle, with the injection pressure monitored by a pore-pressure sensor. Three LVDTs are attached to the top of the light panel, capturing the vertical displacement of the top plate during the fracturing process. A white light panel, right and left circular polarizers form a dark-field circular polariscope. bright-field and dark-field videos are captured by cameras placed underneath the cell.

116  $I = 0.65$  in the blue channel of the dark-field images is adopted here as the threshold to  
 117 differentiate between the two regimes. We analyze the time evolution of the air-oil interface  
 118 morphology from bright-field images, and the rheological behavior of the granular pack from  
 119 dark-field images (see supplemental videos corresponding to the conditions in Fig. 2 and see  
 120 Appendix A for the complete visual phase diagram for a range of values of  $\phi_0$  and  $W$ ). We  
 121 compute the ratio between viscous and capillary forces in the experiments as the modified  
 122 capillary number  $\text{Ca}^* = \eta q R / (\gamma h d^2)$  [22], where oil viscosity  $\eta = 9.71 \text{ Pa}\cdot\text{s}$ , injection rate  
 123  $q = 100 \text{ mL/min}$ , cell radius  $R = 10.6 \text{ cm}$ , interfacial tension  $\gamma = 0.034 \text{ N/m}$ , cell height  
 124  $h = 2 \text{ mm}$ , and particle diameter  $d = 2 \text{ mm}$ , resulting in  $\text{Ca}^* = 6.3 \times 10^3$ . Therefore the  
 125 effect of capillarity is negligible and viscous effects are dominant in our experiments.

126 *Regime I: Fracturing in fluid-filled elastic media.* When particles have been densely  
127 packed initially, air initially invades into the granular pack by expanding a small cavity at  
128 the injection port, with the injection pressure  $P_{\text{inj}}$  ramping up during this period [Fig. 3(a)(d)  
129 for  $\phi_0 = 0.84$ ]. The onset of fracturing in our cohesionless granular packs is determined by  
130 the viscous force from injection overcoming the frictional resistance between particles in the  
131 granular pack. Before fracturing, the injection pressure increases, and this pressure increase  
132 leads to an increased viscous force and, simultaneously, a decreased interparticle frictional  
133 force from the lifting of the top plate—a combination that results in the emergence and  
134 growth of fractures. Higher  $W$  results in higher peak pressure [Fig. 3(a)], and thus the  
135 fracture network becomes more vigorous with well-developed branches (see Appendix A).  
136 In this regime, the effective stress field exhibits a surprising and heretofore unrecognized  
137 phenomenon: behind the propagating fracture tips, an *effective stress shadow*, where the  
138 intergranular stress is low and the granular pack exhibits undrained behavior, emerges and  
139 evolves as fractures propagate [Fig. 2(a), right].

140 *Regime II: Viscous fingering in frictional fluids.* For granular packs with lower initial  
141 packing density ( $\phi_0 = 0.78$ ), the system's rheology is akin to a frictional fluid [18, 28],  
142 as evidenced by the weak or negligible photoelastic response at breakthrough [Fig. 2(b),  
143 right]. The high-viscosity defending fluid inhibits the injected air from infiltrating into pore  
144 spaces [16]. The fluid-filled granular medium effectively behaves like a suspension [36], the  
145 morphology of which is dominated by the Saffman–Taylor instability [18, 37, 38].

146 The temporal evolution of the injection pressure and the vertical displacement of the top  
147 plate encode the information to help understand the interplay between particle movement  
148 and fluid-fluid displacement. At a high injection rate, the dynamics is dominated by the  
149 viscous response to the flow in the cell [22]. For all the confining weights, the injection  
150 pressure exhibits a peak followed by a decay, and a sharp drop corresponding to breakthrough  
151 of air at the cell boundary [Fig. 3(a)]. There are three ways to accommodate the injected  
152 air volume: compressing particles, driving defending fluid out of the cell, and lifting the  
153 confining weight to create extra vertical room. This last mechanism is favored under our  
154 experimental conditions, with injection pressure values  $\sim 30$  kPa. As shown in Fig. 3(b)  
155 where we plot the temporal evolution of the top plate's vertical displacement  $\delta h$  (normalized  
156 by the grain size  $d$ ), the top plate is indeed lifted noticeably during fracturing:  $\delta h/d =$   
157 5%, 6%, 8% under  $W = 25$  N, 65 N, 85 N, respectively. For the fracturing experiments at

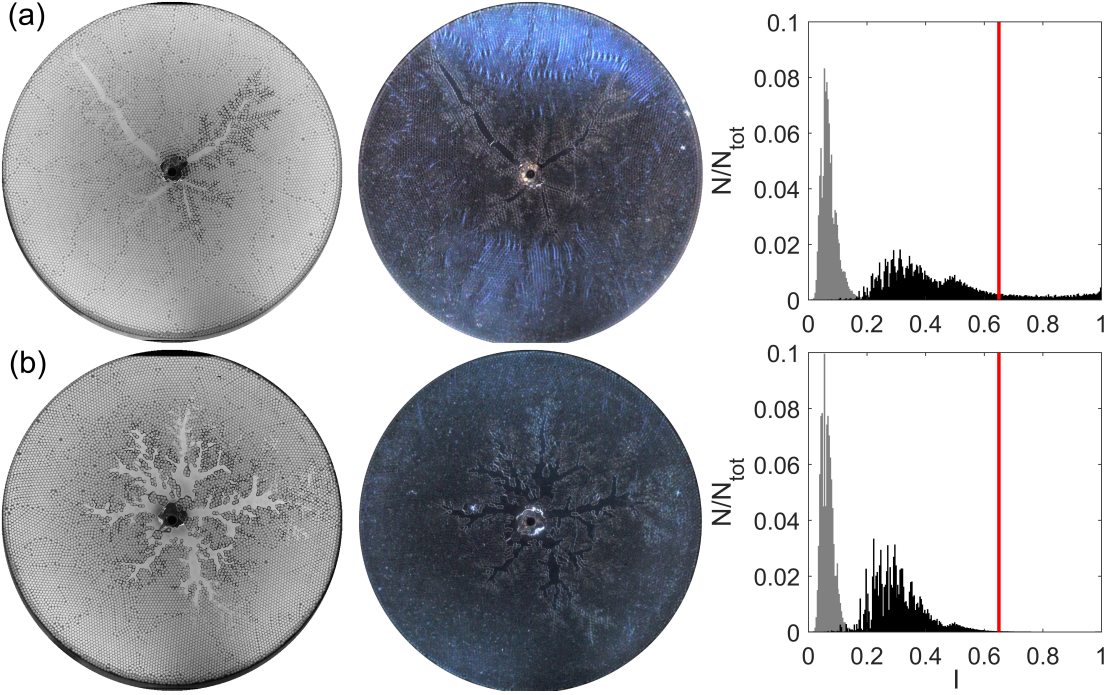


FIG. 2. Bright-field (left), dark-field (middle) images of the invading fluid morphology at breakthrough, and histogram (right) of light intensity of the blue channel of the dark-field image before air injection (in gray color), and at breakthrough (in black color), corresponding to two different initial packing densities  $\phi_0$ , with confining weight  $W = 25$  N. From the dark-field images that visualize the effective stress field, the invading morphology and rheology of the granular packs are classified as: (a) fracturing in fluid-filled elastic media, with strong photoelastic response ( $I > 0.65$ ),  $\phi_0 = 0.84$ , or (b) viscous fingering in frictional fluids, with weak or negligible photoelastic response ( $I < 0.65$ ),  $\phi_0 = 0.78$ . Behind the propagating fracture tips, the effective stress field exhibits an evolving “effective stress shadow”, where the intergranular stress is low and the granular pack exhibits undrained behavior. See supplemental videos for the evolution of the morphology in each regime.

<sup>158</sup>  $\phi_0 = 0.84$ , the initial cell height ( $h_0$ ) is  $0.98d, 0.96d, 0.95d$  under  $W = 25$  N, 65 N, 85 N,  
<sup>159</sup> respectively (see Appendix B for detailed calculations). As  $W$  increases, a higher injection  
<sup>160</sup> pressure is reached before the top plate is lifted [Fig. 3(a)], which stores a larger amount  
<sup>161</sup> of air for fracturing. The invasion morphology at breakthrough [Fig. ??] shows that, for  
<sup>162</sup> larger  $W$ , a larger volume of air is injected into the cell by either fracture branches or pore  
<sup>163</sup> invasion, both of which contribute to lifting the top plate. During air injection, while all

164 the particles are in contact with both the top and bottom plates ( $h(t) < d$ ), the confining  
165 weight is balanced by contact forces between particles and plates and the integrated pore  
166 pressure force across the Hele-Shaw cell. When the top plate is lifted to  $h(t) > d$ , the vertical  
167 component of the interparticle force is negligible and the confining weight is balanced by the  
168 integrated pore pressure force only.

169 We determine the spatiotemporal evolution of the packing density and effective stress  
170 fields as described in the Materials and Methods section [Fig. 3(e)(f)]. As fractures propa-  
171 gate, the pack is compacted ahead of the fracture tips, but exhibits a lower packing density  
172 around the fractures, reflecting the moving-average procedure that we use to determine it.  
173 In the fracturing experiments [Fig. ??], we observe an asymmetric fracturing morphology  
174 with four to six fracture branches in total, and with one or two of them propagating faster  
175 and soon reaching the boundary. In an effort to characterize the rheological heterogeneity of  
176 the granular pack robustly and consistently across all the fracturing experiments, we define  
177 the fracture radius ( $r_{\text{frac}}$ ) as the average distance from three representative fracture tips to  
178 the injection port, including both the long fractures that first reach the boundary and one  
179 or two shorter fractures near the injection port. As fractures propagate, the fracture radius  
180 increases, and the effective stress field exhibits marked rheological heterogeneity [Fig. 3(f)].  
181 Behind the fracture tips ( $r < r_{\text{frac}}(t)$ ), we discover an *effective stress shadow*, where the  
182 intergranular stress is low and the granular pack exhibits undrained behavior. Ahead of  
183 the fracture tips ( $r > r_{\text{frac}}(t)$ ), particles in the annular region are compacted and behave  
184 elastically. For the annular region, this distinct rheological behavior from a frictional to  
185 an elastic response can be understood as a *jamming transition* [39, 40]. This is further  
186 evidenced by the temporal evolution of the averaged packing density and effective stress in  
187 the annular region outside fractures,  $\phi_{\text{out}}$  and  $\sigma'_{\text{out}}$  [Fig. 3(c)], both of which rise above a  
188 background value at the critical point of mechanical stability ( $\phi_c, \sigma'_c$ ) [28, 39–41]. To show  
189 that fracturing is indeed the result of the transition to a solid-like rheological behavior, we  
190 analyzed the evolution of the packing fraction as a function of radial distance,  $\phi(r)$ , at dif-  
191 ferent times, alongside the position of the fracture tip, for one of the fracturing experiments  
192 ( $\phi_0 = 0.84, W = 25 \text{ N}$ ; Fig. 4). The initial packing fraction is sufficiently close to the crit-  
193 ical packing fraction  $\phi_c$  that a relatively minor compaction elicits the formation and initial  
194 propagation of a fracture. The granular pack jams sometime between  $t_{ii} \sim t_{iii}$ , after which  
195 the fracture tip travels across the outer annular region, which is all above  $\phi_c$ .

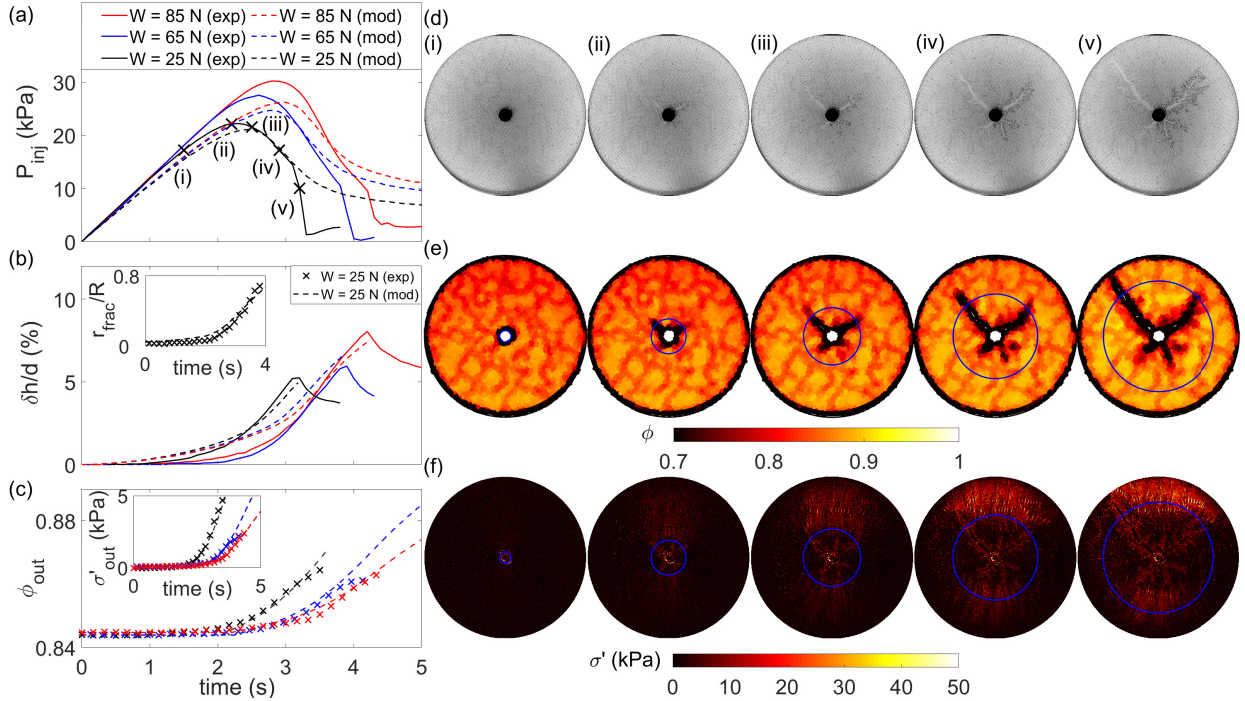


FIG. 3. Time evolution of (a) injection pressure  $P_{\text{inj}}$ , (b) normalized vertical displacement of the top plate  $\delta h/d$ , and (c) the averaged packing density  $\phi_{\text{out}}$  in the annular region outside fractures for experiments with initial packing density  $\phi_0 = 0.84$ , and  $W = 25$  N, 65 N, 85 N. Insets of (b), (c) show the time evolution of the normalized fracture radius  $r_{\text{frac}}/R$ , and the averaged effective stress  $\sigma'_{\text{out}}$  in the annular region outside fractures. The modeling results are plotted in dashed lines. For the experiment with  $\phi_0 = 0.84$  and  $W = 25$  N, a sequence of snapshots shows the time evolution of (d) interface morphology, (e) packing density field, and (f) effective stress field, where the radius of the blue circle represents the fracture radius ( $r_{\text{frac}}$ ) averaged from three representative fracture tips.

196 Where does the effective stress shadow come from? And how does the rheology of a gran-  
 197 ular medium evolve during the fracturing process? To answer these questions, we hypoth-  
 198 esize that the evolving effective stress shadow—the exhibited undrained behavior—stems  
 199 from the buildup of pore pressure within the wedges of granular media between propagat-  
 200 ing fractures. The hypothesis emphasizes the strong coupling between fluid flow and solid  
 201 mechanics underpinning the fracturing process.

202 To analyze the spatiotemporal evolution of the pore pressure, we develop a mechanis-  
 203 tic model for a representative fracture wedge with an angle  $\theta$ —a sector of the fluid-filled

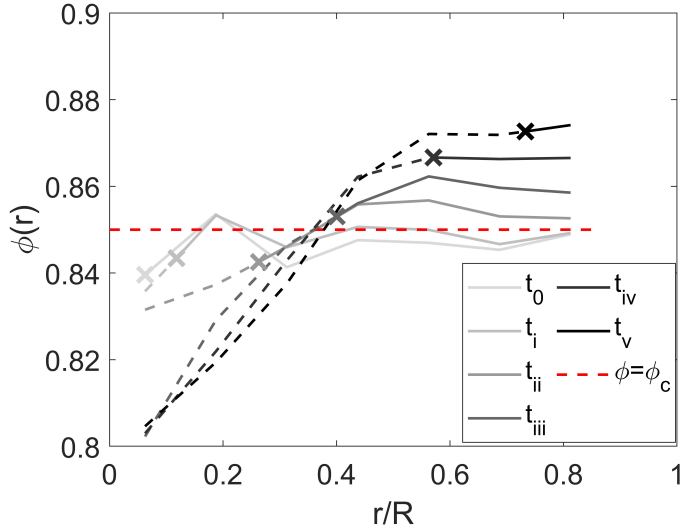


FIG. 4. Radial distribution of the packing fraction ( $\phi(r)$ ) for the fracturing experiment with  $\phi_0 = 0.84$ ,  $W = 25$  N. The temporal evolution of  $\phi(r)$  is plotted at six time instances,  $t_0$  at  $t = 0$ , and  $t_i \sim t_v$  in Fig. 3. The location of the fracture tip is indicated with the cross marker. The packing fraction distribution behind the fracture tip is plotted in dashed lines, and ahead of the fracture tip in solid lines. The red dashed line shows the packing fraction at the jamming transition,  $\phi = \phi_c = 0.85$ .

204 granular medium delineated by two fractures originating from the cell center [Fig. 5(a)].  
 205 We assume Hertz–Mindlin contacts [42] between particles and the plates, and calculate the  
 206 initial vertical compression of the granular pack under the confining weight ( $h_0 < d$ ). We  
 207 model the fracturing process until breakthrough. The proposed model for a representa-  
 208 tive fracture wedge with an angle  $\theta$  solves the time evolution of four unknowns: (1) the  
 209 injection pressure  $P_{\text{inj}}(t)$ ; (2) the height of the granular pack  $h(t)$ ; (3) the length of the  
 210 fracture  $r_{\text{frac}}(t)$ ; and (4) the azimuthally dependent pore pressure field  $p(r, \theta, t)$ . The set  
 211 of governing equations, along with their derivation and working modeling assumptions, is  
 212 included in Appendix B.

213 The modeling results of  $P_{\text{inj}}$ ,  $h$  and  $r_{\text{frac}}$  for different confining weights show good agree-  
 214 ment with the experimental data [Fig. 3(a)(b)]. The time evolution of the pore pressure field  
 215 during fracturing provides important clues to decipher the system’s behavior [Fig. 5(c)]. The  
 216 flow velocity field demonstrates a highly inhomogeneous distribution of the pore pressure  
 217 gradient, which concentrates near the fracture tips [Fig. 5(b)]. The model captures the

218 pressure build-up inside the fracture radius, resulting in the aforementioned “effective stress  
 219 shadow”, a region in which the granular pack is under near-undrained conditions. These flu-  
 220 idized particles in the stress shadow lead to grain compaction in the annular region outside,  
 221 which helps explain the distinct rheological behavior from a frictional to an elastic response  
 222 [Fig. 5(a)].

223 With the insights from the pore pressure model, we expect a different fluid-flow behavior  
 224 in the loose and dense regions of the granular pack: a granular–fluid mixture behind the  
 225 fracture tips, and an elastic medium ahead of the fracture tips. The homogeneous granular  
 226 pack assumption in the pressure model (Appendix B) does not reflect the disparate rheology.  
 227 For the rheology model, we take an effective permeability  $k'$  [43] and viscosity  $\eta'$  [36] for  
 228 the granular–fluid mixture within the fracture radius and approximate the number of parti-  
 229 cles  $N_{\delta t}$  entering the annular region within a timestep as  $N_{\delta t} = (v_p \delta t / d) \cdot [r_{\text{frac}}(t) \theta / d]$ , with  
 230  $v_p = -(k' / \eta') (\partial p / \partial r)|_{r=r_{\text{frac}}(t)}$ , where  $v_p$  is the particle flow velocity at the fracture radius.  
 231 We update the two-dimensional packing density in the annular region as

$$\phi(t + \delta t) = \phi(t) + \frac{N_{\delta t} \frac{\pi d^2}{4}}{\frac{1}{2}(R^2 - (r_{\text{frac}}(t))^2)\theta}. \quad (1)$$

232 To infer the effective stress from the packing density, we adopt the power-law constitutive  
 233 relationship  $\sigma' - \sigma'_c = K \left( \frac{\phi - \phi_c}{\phi_c} \right)^\psi$  [39, 40, 44–46]. The modeling results of  $(\phi(t), \sigma'(t))$   
 234 in the annular region agree well with the experiments [Fig. 3(c)], capturing both the pore  
 235 pressure evolution and rheology of the granular medium. A detailed account of the modeling  
 236 parameters is included in Appendix B.

237 To explore the rheological properties of the granular medium in the annulus, we conduct  
 238 the jamming transition analysis for the fracturing experiments. We determine the jamming  
 239 transition  $\phi_c$  from the time evolution of the effective stress  $\sigma'$  as the intersection of two  
 240 straight lines: one fitting the response of the background state, and one fitting the asymptotic  
 241 behavior in the highly compacted state [28, 40, 47] [Fig. 6(a)]. We find that  $\phi_c$  lies in the  
 242 range 0.83–0.85 for the fracturing experiments [Fig. 2(a), and regime I in Appendix A], with  
 243 higher  $\phi_c$  corresponding to denser granular packs. The experimental value of  $\phi_c$  is consistent  
 244 with the theoretical prediction that the system jams at the random close packing density  
 245  $\phi_c \approx \phi_{\text{rcp}} \approx 0.84$  [28, 48–50]. We synthesize the elastic response of the system by plotting  
 246 the effective stress against the packing density, showing that, above  $\phi_c$ ,  $\sigma'$  follows a power-  
 247 law increase,  $\sigma' - \sigma'_c \sim (\phi - \phi_c)^\psi$ , with the exponent  $\psi$  in the range 1.1–1.5 [Fig. 6(b)]. As

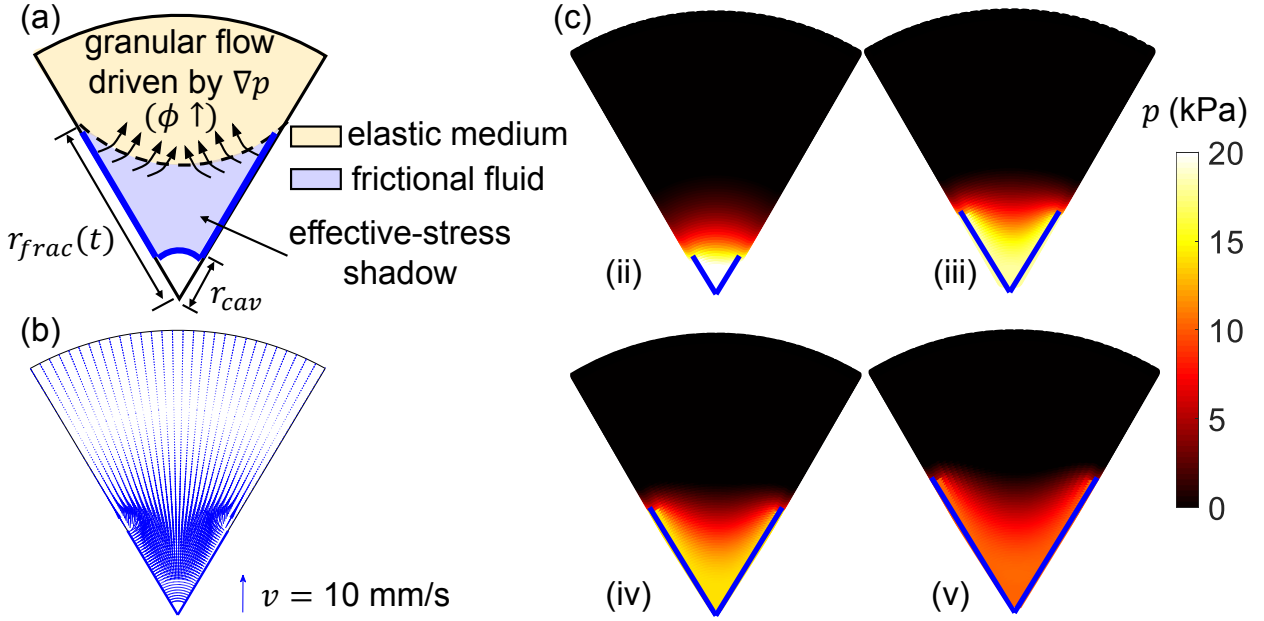


FIG. 5. A mechanistic model on fracturing that explains the effective stress shadow observed in experiments. (a) Schematic of the model setup for a fracture wedge with an angle  $\theta = 60^\circ$ . The granular flow driven by the concentrated pore pressure gradient within fracture tips keeps compacting particles in the annular region outside, leading to its increase in packing density and a rheological transition from frictional flow to elastic medium. (b) Modeled flow velocity field at time instance (iii) in Fig. 3(a). (c) Sequence of snapshots showing the time evolution of the modeling pore pressure field. Modeling conditions:  $\phi_0 = 0.84$ ,  $W = 25$  N,  $q = 100$  mL/min, and  $V_0 = 15$  mL.

confirmed in previous studies [28, 39, 40, 44, 45], the value of  $\psi$  lies between the value for linear ( $\psi = 1.0$ ) and Hertzian contacts ( $\psi = 1.5$ ). In our stress-strain diagram [Fig. 6(b)], the elastic response in the annular region indicates a value of  $K \sim 200$  to 300 kPa, which is close to the value measured in separate experiments [30]. Ideally, the parameters in the constitutive relation ( $K, \psi$ ) would be the same for all the experiments, reflecting the material's elastic behavior after the jamming transition. In the experiments, though, this is not the case, and the coefficients in the power law exhibit some variability in part at least due to the asymmetric fracturing morphology and the inhomogeneous distribution of the packing fraction and effective stress fields ahead of the fracture tips. In an effort to characterize the rheological heterogeneity of the granular pack more robustly, in our mathematical model we define the fracture radius ( $r_{\text{frac}}$ ) as the averaged distance from three representative fracture

261 tips to the injection port.

## 262 CONCLUSIONS

263 In summary, we have studied the morphology and rheology of injection-induced fracturing  
264 in wet granular packs via a recently developed experimental technique, photoporomechanics,  
265 which extends photoelasticity to granular systems with a fluid-filled connected pore space  
266 [30]. Experiments of air injection into photoelastic granular packs with different initial pack-  
267 ing densities and confining weights have led us to uncover two invasion regimes: fracturing  
268 in fluid-filled elastic media, and viscous fingering in frictional fluids. Visualizing the evolving  
269 effective stress field using photoporomechanics, we discover that behind the fracture tips,  
270 an *effective stress shadow*—where the intergranular stress is low and the granular pack ex-  
271 hibits undrained behavior—evolves as fractures propagate. With a mechanistic model for  
272 a fracture wedge, we capture the fluid pressure build-up inside the shadow region. We de-  
273 velop a rheology model that explains both the effective stress shadow behind the fracture  
274 tips, and the distinct rheological behavior from a frictional to an elastic response for the  
275 granular medium outside the fractures. Finally, we rationalize the emergence of fracturing  
276 across our experiments as a jamming transition initially proposed in the context of coupled  
277 pore-network/discrete-element models [28].

278 Our study paves the way for understanding the mechanical and fracture properties of  
279 porous media that are of interest for many field applications, including plant root growth in  
280 granular material [31, 51], powder aggregation [52], rock mechanics [53], soil rheology [54],  
281 and geoengineering [55]. We demonstrate that photoporomechanics serves as a promising  
282 technique to study coupled fluid-solid processes in granular media [4] and may provide  
283 fundamental insights on specific applications, including energy recovery [56], gas venting  
284 [57], and geohazards [58].

285 Y.M. and W.L. contributed equally to this work. This work was supported by the U.S.  
286 Department of Energy (Grant No. DE-SC0018357) and the U.S. National Science Founda-  
287 tion (Grant No. CMMI-1933416).

288 **Appendix A: The Complete Visual Phase Diagram of Invading Fluid Morphology**  
289 **at Breakthrough**

290 Figure 7 shows the complete visual phase diagram of invading fluid morphology for a  
291 range of values of  $\phi_0$  and  $W$ .

292 **Appendix B: Mathematical Model of Coupled Fluid Pressure and Granular Me-  
293 chanics**

294 We develop a mechanistic model for a representative fracture wedge with an angle  $\theta_0$ .  
295 We assume Hertz–Mindlin contacts [42] between particles and the plates, and calculate the  
296 initial vertical compression of the granular pack under the confining weight ( $h_0 < d$ ). We  
297 model the fracturing process until breakthrough of the injected fluid. The model solves the  
298 time evolution of four unknowns: (1) the injection pressure  $P_{\text{inj}}(t)$ ; (2) the height of the  
299 granular pack  $h(t)$ ; (3) the length of the fracture  $r_{\text{frac}}(t)$ ; and (4) the azimuthally dependent  
300 pore pressure field during fracturing,  $p(r, \theta, t)$ .

301 **Governing equations**

302 1. We assume fluid flowing in a homogeneous porous medium of uniform packing den-  
303 sity ( $\phi_{3d}$ ), and time dependent uniform thickness ( $h(t)$ ), in an azimuthally dependent  
304 manner. We perform a mass balance on an annulus sector between  $r$  and  $r + \delta r$ ,  $\theta$   
305 and  $\theta + \delta\theta$  (Fig. 8) for the incompressible defending fluid (silicone oil):

$$306 \rho_f(v_r r \delta\theta h - v_{r+\delta r} (r + \delta r) \delta\theta h + v_\theta \delta r h - v_{\theta+\delta\theta} \delta r h) = \frac{\partial(\rho_f r \delta r \delta\theta h (1 - \phi_{3d}))}{\partial t} \quad (\text{B. 1})$$

307 where  $\phi_{3d}$  is the three-dimensional packing density of the granular pack, which is  
308 computed as the ratio between the volume of particles, and the cell volume saturated  
309 with the defending silicone oil. Before the air injection,  $\phi_{3d} = \frac{V_s}{V_t} = \frac{M_s/\rho_s}{\pi R^2 h_0}$ , where  
310  $M_s$  and  $\rho_s$  are the mass and density of photoelastic particles in a granular pack,  
311 respectively. The initial cell height,  $h_0$ , is calculated from the confining weight by  
312 assuming Hertzian contacts between the particles and the glass plate. We estimate  
313 the 3D packing density before air injection and also at breakthrough, a calculation  
314 that shows a negligible difference between the two values. Therefore, in the model, we

315 take the 3D packing fraction as a constant calculated with the initial cell height,  $\phi_{3d,0}$ .  
 316 Dividing the equation by  $\rho_f \delta r \delta \theta$ , and letting  $\delta r \rightarrow 0$ ,  $\delta \theta \rightarrow 0$ :

317 
$$-\frac{\partial(v_r rh)}{\partial r} - \frac{\partial(v_\theta h)}{\partial \theta} = \frac{\partial(rh(1 - \phi_{3d}))}{\partial t}, \quad (\text{B. 2})$$

318 Combining with Darcy's law for the fluid velocity, we obtain:

319 
$$\frac{\partial(rh \frac{k}{\eta} \frac{\partial p}{\partial r})}{\partial r} + \frac{\partial(\frac{h}{r} \frac{k}{\eta} \frac{\partial p}{\partial \theta})}{\partial \theta} = \frac{\partial(rh(1 - \phi_{3d}))}{\partial t}, \quad (\text{B. 3})$$

320 where  $k$  is the permeability of the granular pack and  $\eta$  is the viscosity of the defending  
 321 fluid. We assume  $\phi_{3d}$ ,  $k$ ,  $\eta$  to be constant in space and time. We then obtain the pres-  
 322 sure diffusion equation for the defending fluid (silicone oil) in cylindrical coordinates  
 323 as follows:

324 
$$\frac{kh}{\eta} \left( \frac{\partial^2 p}{\partial r^2} + \frac{1}{r} \frac{\partial p}{\partial r} + \frac{1}{r^2} \frac{\partial^2 p}{\partial \theta^2} \right) = (1 - \phi_{3d}) \frac{\partial h}{\partial t}, \quad (\text{B. 4})$$

2. Conservation of mass for the total air in the system:

$$P_{\text{inj}}(t)(V_0 - qt + V_{\text{air}}(t)) = P_0(V_0 + \pi r_0^2 h_0), \quad (\text{B. 5})$$

$$V_{\text{air}}(t) = \pi r_0^2 h(t) + V_{\text{frac}}(t), \quad (\text{B. 6})$$

$$V_{\text{frac}}(t) = \frac{2\pi}{\theta_0}(r_{\text{frac}}(t) - r_0)wh(t), \quad (\text{B. 7})$$

325 where  $V_0$  is the syringe volume before air injection,  $r_0$  is the injection port radius,  
 326  $V_{\text{air}}(t)$  is the air volume in the cell that consists of the air volume at the injection port  
 327 and the volume of fractures  $V_{\text{frac}}(t)$ ,  $w$  is the fracture width, and  $P_0$  is the atmospheric  
 328 pressure.

329 3. Assuming incompressible solid grains, conservation of mass for the solid grains states  
 330 that

331 
$$\frac{\partial V_s}{\partial t} = 0 \rightarrow \frac{\partial[(V_t(t) - V_{\text{air}}(t))\phi_{3d}]}{\partial t} = 0, \quad (\text{B. 8})$$

332 where  $V_t(t)$  is the total cell volume. As  $\phi_{3d}$  is a constant with time, the equation  
 333 becomes:

334 
$$V_{\text{air}}(t) = \pi R^2(h(t) - h_0) + \pi r_0^2 h_0, \quad (\text{B. 9})$$

335 where  $R$  is the radius of the cell.

336 4. We establish the quasi-static force balance for the top plate assuming Hertzian contacts  
 337 for the granular pack. When all the particles are in contact with both the top and  
 338 bottom plates ( $h(t) < d$ ), the confining weight is balanced by contact forces between  
 339 particles and plates and the integrated pore pressure force. When the top plate is  
 340 lifted to  $h(t) > d$ , particles have contacts with either the top or bottom plate, and the  
 341 vertical component ( $F_v$ ) of the interparticle force ( $F_p$ ) is negligible from the geometric  
 342 configuration,  $\frac{F_v}{F_p} = \frac{h-d}{d} < 0.03$ , and thus the confining weight is balanced by the  
 343 integrated pore pressure force only:

$$344 K_n \left\langle (d - h(t)) \right\rangle^{\frac{3}{2}} + P_{\text{inj}}(t) \pi r_0^2 + \frac{2\pi}{\theta_0} \int_{r_0}^R \int_{-\frac{\theta_0}{2}}^{\frac{\theta_0}{2}} p(r, \theta, t) r d\theta dr = W, \quad (\text{B. 10})$$

345 where  $K_n$  is the contact normal stiffness of the granular pack under the confining  
 346 weight.

347 **Initial and boundary conditions**

The initial conditions for the four unknowns ( $P_{\text{inj}}(t)$ ,  $h(t)$ ,  $r_{\text{frac}}(t)$ , and  $p(r, \theta, t)$ ) are as follows:

$$P_{\text{inj}}(t = 0) = 0, \quad (\text{B. 11})$$

$$h(t = 0) = h_0 = d - \left(\frac{W}{K_n}\right)^{2/3}, \quad (\text{B. 12})$$

$$r_{\text{frac}}(t = 0) = r_0, \quad (\text{B. 13})$$

$$p(r_0 \leq r \leq R, -\frac{\theta_0}{2} \leq \theta \leq \frac{\theta_0}{2}, t = 0) = 0, \quad (\text{B. 14})$$

The boundary conditions are:

$$p(R, \theta, 0) = 0, \quad (\text{B. 15})$$

$$p(r_0 \leq r \leq r_{\text{frac}}(t), \pm\theta_0/2, t) = p(r_0, \theta, t) = P_{\text{inj}}(t), \quad (\text{B. 16})$$

$$\left. \frac{\partial p}{\partial \theta} \right|_{(r_{\text{frac}}(t) \leq r \leq R, \pm\theta_0/2, t)} = 0, \quad (\text{B. 17})$$

348 **Modeling parameters**

349 A summary of the modeling parameters is shown in Table I. There is no fitting parameter  
 350 in this model. The Hertzian-contact normal stiffness,  $K_n$ , is measured from a separate

TABLE I. Modeling parameters for a mechanistic model of a representative fracture wedge

Symbol	Value	Unit	Variable
$r_0$	2	mm	Injection port radius
$R$	10.6	cm	Hele-Shaw cell radius
$M_s$	40	g	Mass of the photoelastic particles
$\rho_s$	1	g/cm <sup>3</sup>	Density of the photoelastic particles
$\phi_{3d}$	0.58,0.59,0.60		3D packing density under $W = 25, 65, 85$ N
$W$	25,65,85	N	Confining weight acting on the the granular pack
$d$	2	mm	Diameter of the photoelastic particles
$K_n$	9.4e7	Nm <sup>-3/2</sup>	Hertzian contact normal stiffness of the granular pack
$q$	100	mL/min	Air injection rate
$V_0$	15	mL	Air reservoir volume
$P_0$	101	kPa	Atmospheric pressure
$\theta$	$\pi/3$		Angle of a representative fracture wedge
$w$	$3d$	mm	Fracture width
$h_0$	$0.98d, 0.96d, 0.95d$	mm	Initial height of the granular pack under $W = 25, 65, 85$ N
$k$	$(0.08d)^2$	mm <sup>2</sup>	Permeability of the granular pack
$k'$	$d^2/12$	mm <sup>2</sup>	Effective permeability of the granular-fluid mixture
$\eta$	9.71	Pa·s	Defending fluid viscosity
$\eta'$	$9.8\eta$	Pa·s	Effective viscosity of the granular-fluid mixture [36]

351 experiment where we track the vertical displacement of the top plate as the confining weight  
 352 increases from 10 N to 110 N, the permeability of the granular pack,  $k$ , is measured in consol-  
 353 idation experiments [30]. Other parameters are either calculated from the experimental set  
 354 up ( $r_0, R, M_s, \rho_s, \phi_{3d}, W, d, q, V_0, P_0, h_0, k', \eta, \eta'$ ), or directly measured during the fracturing  
 355 experiments ( $w, \theta_0$ ).

356      **Numerical implementation**

357      We use a finite difference numerical scheme to solve the four coupled governing equations  
358      [B. 4, 5, 9 and 10]. The numerical implementation scheme for the mathematical model is  
359      shown in Fig. 9. The fluid pressure is fully coupled with granular mechanics by solving the  
360      unknown variables,  $h(t)$  and  $r_{\text{frac}}(t)$ , iteratively until convergence at each time step.

---

362      \* juanes@mit.edu

363      [1] David E Hill and J-Y Parlange, “Wetting front instability in layered soils,” *Soil Sci. Soc. Am. J.* **36**, 697–702 (1972).

364      [2] Guillaume T Charras, Justin C Yarrow, Mike A Horton, L Mahadevan, and TJ Mitchison, “Non-equilibration of hydrostatic pressure in blebbing cells,” *Nature* **435**, 365–369 (2005).

365      [3] Michael L Szulczewski, Christopher W MacMinn, Howard J Herzog, and Ruben Juanes, “Lifetime of carbon capture and storage as a climate-change mitigation technology,” *Proc. Natl. Acad. Sci. U.S.A.* **109**, 5185–5189 (2012).

366      [4] Ruben Juanes, Yue Meng, and Bauyrzhan K Primkulov, “Multiphase flow and granular mechanics,” *Phys. Rev. Fluids* **5**, 110516 (2020).

367      [5] A. Groisman and E. Kaplan, “An experimental study of cracking induced by desiccation,” *Europhys. Lett.* **25**, 415–420 (1994).

368      [6] H. Shin and J. C. Santamarina, “Desiccation cracks in saturated fine-grained soils: particle-level phenomena and effective-stress analysis,” *Geotechnique* **61**, 961–972 (2011).

369      [7] Eric R Dufresne, Eric I Corwin, NA Greenblatt, Jacqueline Ashmore, DY Wang, Anthony D Dinsmore, JX Cheng, XS Xie, John W Hutchinson, and David A Weitz, “Flow and fracture in drying nanoparticle suspensions,” *Phys. Rev. Lett.* **91**, 224501 (2003).

370      [8] Dominic Vella, Pascale Aussillous, and L Mahadevan, “Elasticity of an interfacial particle raft,” *Europhys. Lett.* **68**, 212 (2004).

371      [9] AK Jain and R Juanes, “Preferential mode of gas invasion in sediments: Grain-scale mechanistic model of coupled multiphase fluid flow and sediment mechanics,” *J. Geophys. Res. Solid Earth* **114**, B08101 (2009).

384 [10] Hosung Shin and J Carlos Santamarina, “Fluid-driven fractures in uncemented sediments:  
385 Underlying particle-level processes,” *Earth Planet. Sci. Lett.* **299**, 180–189 (2010).

386 [11] Lucas Goehring, William J Clegg, and Alexander F Routh, “Plasticity and fracture in drying  
387 colloidal films,” *Phys. Rev. Lett.* **110**, 024301 (2013).

388 [12] Christian Peco, Wei Chen, Yingjie Liu, MM Bandi, John E Dolbow, and Eliot Fried, “Influ-  
389 ence of surface tension in the surfactant-driven fracture of closely-packed particulate mono-  
390 layers,” *Soft Matter* **13**, 5832–5841 (2017).

391 [13] Zhonghao Sun and J Carlos Santamarina, “Grain-displacive gas migration in fine-grained  
392 sediments,” *J. Geophys. Res. Solid Earth* **124**, 2274–2285 (2019).

393 [14] Bjornar Sandnes, HA Knudsen, KJ Måløy, and EG Flekkøy, “Labyrinth patterns in confined  
394 granular-fluid systems,” *Phys. Rev. Lett.* **99**, 038001 (2007).

395 [15] Xiang Cheng, Lei Xu, Aaron Patterson, Heinrich M Jaeger, and Sidney R Nagel, “Towards  
396 the zero-surface-tension limit in granular fingering instability,” *Nat. Phys.* **4**, 234 (2008).

397 [16] Haiying Huang, Fengshou Zhang, Patrick Callahan, and Joseph Ayoub, “Granular fingering  
398 in fluid injection into dense granular media in a hele-shaw cell,” *Phys. Rev. Lett.* **108**, 258001  
399 (2012).

400 [17] Fengshou Zhang, Branko Damjanac, and Haiying Huang, “Coupled discrete element modeling  
401 of fluid injection into dense granular media,” *J. Geophys. Res. Solid Earth* **118**, 2703–2722  
402 (2013).

403 [18] Bjornar Sandnes, EG Flekkøy, HA Knudsen, KJ Måløy, and H See, “Patterns and flow in  
404 frictional fluid dynamics,” *Nat. Commun.* **2**, 288 (2011).

405 [19] Benjamin P Scandella, Liam Pillsbury, Thomas Weber, Carolyn Ruppel, Harold F Hemond,  
406 and Ruben Juanes, “Ephemerality of discrete methane vents in lake sediments,” *Geophys.*  
407 *Res. Lett.* **43**, 4374–4381 (2016).

408 [20] Tad W Patzek, Frank Male, and Michael Marder, “Gas production in the barnett shale obeys  
409 a simple scaling theory,” *Proc. Natl. Acad. Sci. U.S.A.* **110**, 19731–19736 (2013).

410 [21] J Mataix-Solera, V Arcenegui, N Tessler, R Zornoza, L Wittenberg, C Martínez, P Caselles,  
411 A Pérez-Bejarano, D Malkinson, and MM Jordán, “Soil properties as key factors controlling  
412 water repellency in fire-affected areas: Evidences from burned sites in spain and israel,” *Catena*  
413 **108**, 6–13 (2013).

414 [22] Ran Holtzman, Michael L Szulczewski, and Ruben Juanes, “Capillary fracturing in granular  
415 media,” Phys. Rev. Lett. **108**, 264504 (2012).

416 [23] Ran Holtzman and Ruben Juanes, “Crossover from fingering to fracturing in deformable  
417 disordered media,” Phys. Rev. E **82**, 046305 (2010).

418 [24] Benoit Carrier and Sylvie Granet, “Numerical modeling of hydraulic fracture problem in  
419 permeable medium using cohesive zone model,” Eng. Fract. Mech. **79**, 312–328 (2012).

420 [25] Brice Lecampion and Jean Desroches, “Simultaneous initiation and growth of multiple radial  
421 hydraulic fractures from a horizontal wellbore,” J. Mech. Phys. Solids **82**, 235–258 (2015).

422 [26] Andro Mikelic, Mary F Wheeler, and Thomas Wick, “A phase-field method for propagating  
423 fluid-filled fractures coupled to a surrounding porous medium,” Multiscale Model. Simul. **13**,  
424 367–398 (2015).

425 [27] David Santillán, Ruben Juanes, and Luis Cueto-Felgueroso, “Phase field model of hydraulic  
426 fracturing in poroelastic media: Fracture propagation, arrest, and branching under fluid in-  
427 jection and extraction,” Journal of Geophysical Research: Solid Earth **123**, 2127–2155 (2018).

428 [28] Yue Meng, Bauyrzhan K Primkulov, Zhibing Yang, Chung Yee Kwok, and Ruben Juanes,  
429 “Jamming transition and emergence of fracturing in wet granular media,” Phys. Rev. Res. **2**,  
430 022012 (2020).

431 [29] Francisco J Carrillo and Ian C Bourg, “Capillary and viscous fracturing during drainage in  
432 porous media,” Phys. Rev. E **103**, 063106 (2021).

433 [30] Wei Li, Yue Meng, Bauyrzhan K Primkulov, and Ruben Juanes, “Photo-poromechanics: An  
434 experimental method to visualize the effective stress field in fluid-filled granular media,” Phys.  
435 Rev. Appl. **16**, 024043 (2021).

436 [31] Jonathan Barés, Serge Mora, Jean-Yves Delenne, and Thierry Fourcaud, “Experimental  
437 observations of root growth in a controlled photoelastic granular material,” in *EPJ Web of  
438 Conferences*, Vol. 140 (EDP Sciences, 2017) p. 14008.

439 [32] Karen E Daniels, Jonathan E Kollmer, and James G Puckett, “Photoelastic force measure-  
440 ments in granular materials,” Rev. Sci. Instrum. **88**, 051808 (2017).

441 [33] Michael L Falk and James S Langer, “Dynamics of viscoplastic deformation in amorphous  
442 solids,” Phys. Rev. E **57**, 7192 (1998).

443 [34] L Rothenburg and APS Selvadurai, “A micromechanical definition of the cauchy stress tensor  
444 for particulate media,” in *Mechanics of Structural Media, Proc. of the Int. Symp. on the*

445 *Mechanical Behaviour of Structured Media, Ottawa, Canada, 18–21 May* (Elsevier, 1981) pp.

446 469–486.

447 [35] See Supplemental Material at [URL will be inserted by publisher] for videos corresponding to  
448 the conditions in Fig. 2.

449 [36] D Quemada, “Rheology of concentrated disperse systems and minimum energy dissipation  
450 principle,” *Rheol. Acta* **16**, 82–94 (1977).

451 [37] Philip Geoffrey Saffman and Geoffrey Ingram Taylor, “The penetration of a fluid into a porous  
452 medium or hele-shaw cell containing a more viscous liquid,” *Proc. Math. Phys. Eng. Sci. P*  
453 *Roy Soc A-Math Phys.* **245**, 312–329 (1958).

454 [38] C Chevalier, A Lindner, M Leroux, and E Clément, “Morphodynamics during air injection  
455 into a confined granular suspension,” *J. Non-Newton. Fluid Mech.* **158**, 63–72 (2009).

456 [39] Corey S O’Hern, Leonardo E Silbert, Andrea J Liu, and Sidney R Nagel, “Jamming at zero  
457 temperature and zero applied stress: The epitome of disorder,” *Phys. Rev. E* **68**, 011306  
458 (2003).

459 [40] TS Majmudar, M Sperl, Stefan Luding, and Robert P Behringer, “Jamming transition in  
460 granular systems,” *Phys. Rev. Lett.* **98**, 058001 (2007).

461 [41] Hernan A Makse, Nicolas Gland, David L Johnson, and Lawrence Schwartz, “Granular  
462 packings: Nonlinear elasticity, sound propagation, and collective relaxation dynamics,” *Phys.*  
463 *Rev. E* **70**, 061302 (2004).

464 [42] Kenneth Langstreh Johnson and Kenneth Langstreh Johnson, *Contact Mechanics* (Cam-  
465 bridge university press, 1987).

466 [43] Pijush K Kundu, Ira M Cohen, and D Dowling, *Fluid Mechanics* (Elsevier, 2008).

467 [44] Corey S O’Hern, Stephen A Langer, Andrea J Liu, and Sidney R Nagel, “Random packings  
468 of frictionless particles,” *Phys. Rev. Lett.* **88**, 075507 (2002).

469 [45] Leonardo E Silbert, Deniz Ertas, Gary S Grest, Thomas C Halsey, and Dov Levine, “Geometry  
470 of frictionless and frictional sphere packings,” *Phys. Rev. E* **65**, 031304 (2002).

471 [46] Christopher W MacMinn, Eric R Dufresne, and John S Wettlaufer, “Fluid-driven deformation  
472 of a soft granular material,” *Phys. Rev. X* **5**, 011020 (2015).

473 [47] Claus Heussinger and Jean-Louis Barrat, “Jamming transition as probed by quasistatic shear  
474 flow,” *Phys. Rev. Lett.* **102**, 218303 (2009).

475 [48] James G Berryman, “Random close packing of hard spheres and disks,” Phys. Rev. A **27**,  
476 1053 (1983).

477 [49] Massimo Pica Ciamarra, Raffaele Pastore, Mario Nicodemi, and Antonio Coniglio, “Jamming  
478 phase diagram for frictional particles,” Phys. Rev. E **84**, 041308 (2011).

479 [50] Ning Xu, Jerzy Blawdziewicz, and Corey S O’Hern, “Random close packing revisited: Ways  
480 to pack frictionless disks,” Phys. Rev. E **71**, 061306 (2005).

481 [51] DM Wendell, K Luginbuhl, J Guerrero, and AE Hosoi, “Experimental investigation of plant  
482 root growth through granular substrates,” Exp. Mech. **52**, 945–949 (2012).

483 [52] Kevin Kendall and Carl Stainton, “Adhesion and aggregation of fine particles,” Powder Technol.  
484 **121**, 223–229 (2001).

485 [53] John Conrad Jaeger, Neville GW Cook, and Robert Zimmerman, *Fundamentals of Rock  
486 Mechanics* (John Wiley & Sons, 2009).

487 [54] James Kenneth Mitchell and Kenichi Soga, *Fundamentals of Soil Behavior*, Vol. 3 (John Wiley  
488 & Sons New York, 2005).

489 [55] Donald L Turcotte, Eldridge M Moores, and John B Rundle, “Super fracking,” Phys. Today  
490 **67**, 34 (2014).

491 [56] Ebrahim Ghanbari and Hassan Dehghanpour, “The fate of fracturing water: A field and  
492 simulation study,” Fuel **163**, 282–294 (2016).

493 [57] Adam Skarke, Carolyn Ruppel, M Kodis, D Brothers, and E Lobecker, “Widespread methane  
494 leakage from the sea floor on the northern us atlantic margin,” Nat. Geosci. **7**, 657–661 (2014).

495 [58] A. L. Handwerger, A. W. Rempel, R. M. Skarbek, J. J. Roering, and G. E. Hilley, “Rate-  
496 weakening friction characterizes both slow sliding and catastrophic failure of landslides,” Proc.  
497 Natl. Acad. Sci. U.S.A. **113**, 10281–10286 (2016).

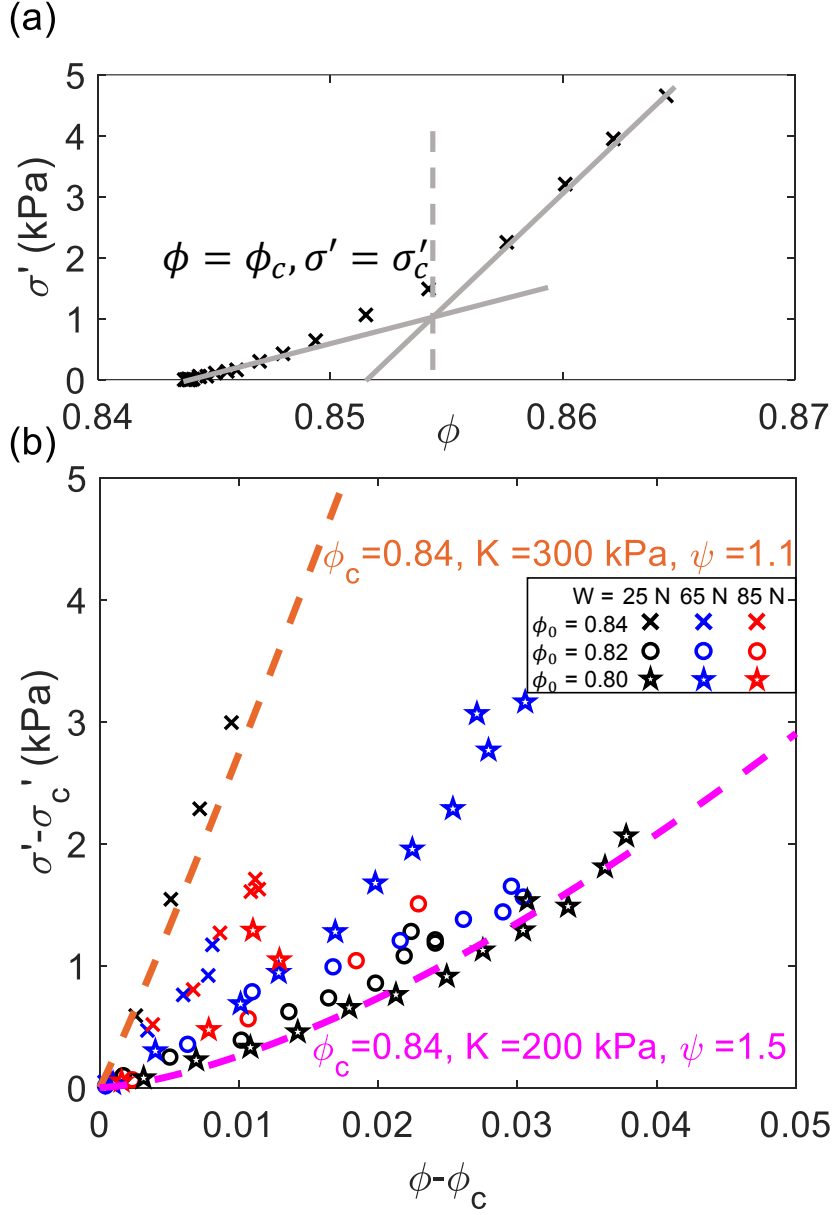


FIG. 6. Jamming transition analysis for the fracturing experiments ( $\phi_0 = 0.84, 0.82, 0.80, W = 25$  N, 65 N, 85 N). (a) Determination of the critical packing density and effective stress at jamming for the experiment  $W = 25$  N,  $\phi_0 = 0.84$ . (b)  $\sigma' - \sigma'_c$  plotted against  $\phi - \phi_c$  for the fracturing experiments, which follows the power-law constitutive relationship  $\sigma' - \sigma'_c = K \left( \frac{\phi - \phi_c}{\phi_c} \right)^\psi$  [39, 40, 44–46].

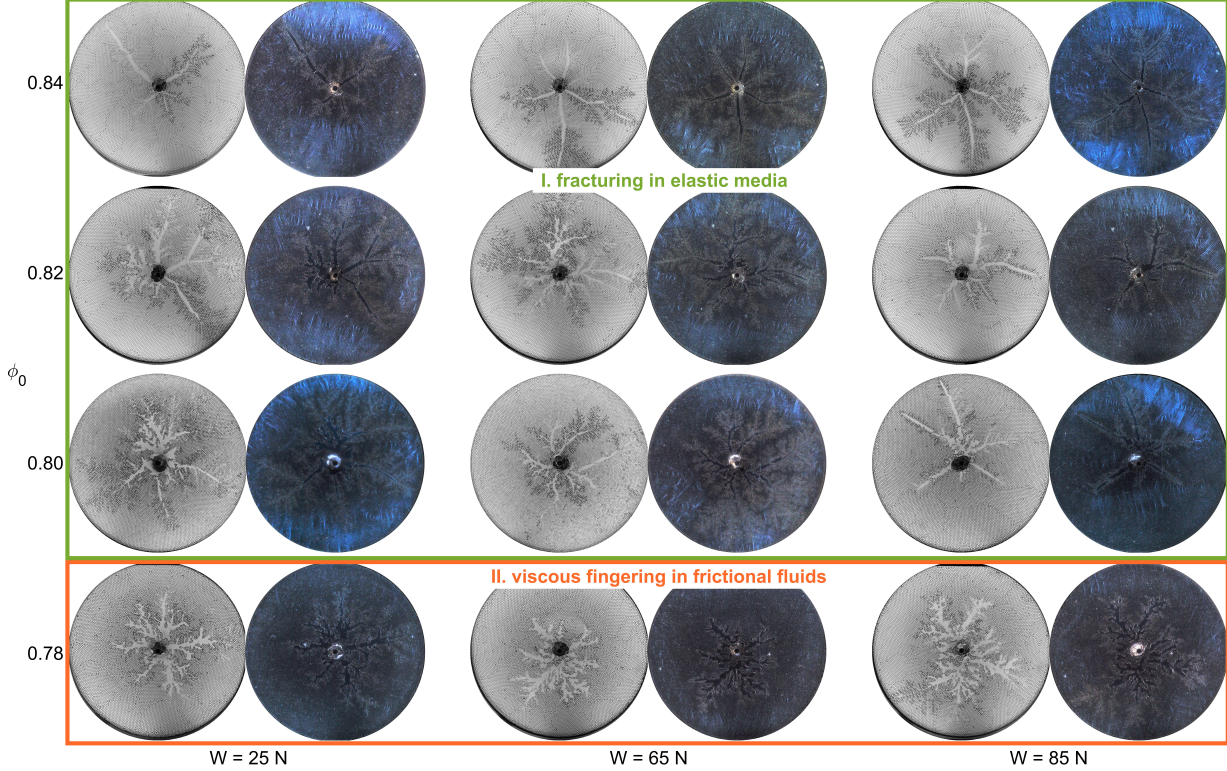


FIG. 7. Visual phase diagram of the bright-field (left) and dark-field (right) invading fluid morphology at breakthrough corresponding to different confining weights  $W$  and initial packing densities  $\phi_0$ . From dark-field images that visualize the effective stress field, the invading morphology and rheology of the granular packs is classified as fracturing in fluid-filled elastic media (with strong photoelastic response,  $\phi_0 = 0.84, 0.82, 0.80$ ), or viscous fingering in frictional fluids (with weak or negligible photoelastic response,  $\phi_0 = 0.78$ ). Behind the propagating fracture tips, the effective stress field exhibits an evolving “effective stress shadow”, where the intergranular stress is low and the granular pack exhibits undrained behavior.

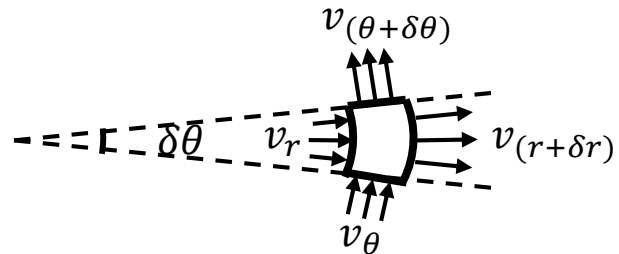


FIG. 8. An annulus sector used to derive the pressure diffusion equation in radial coordinates.

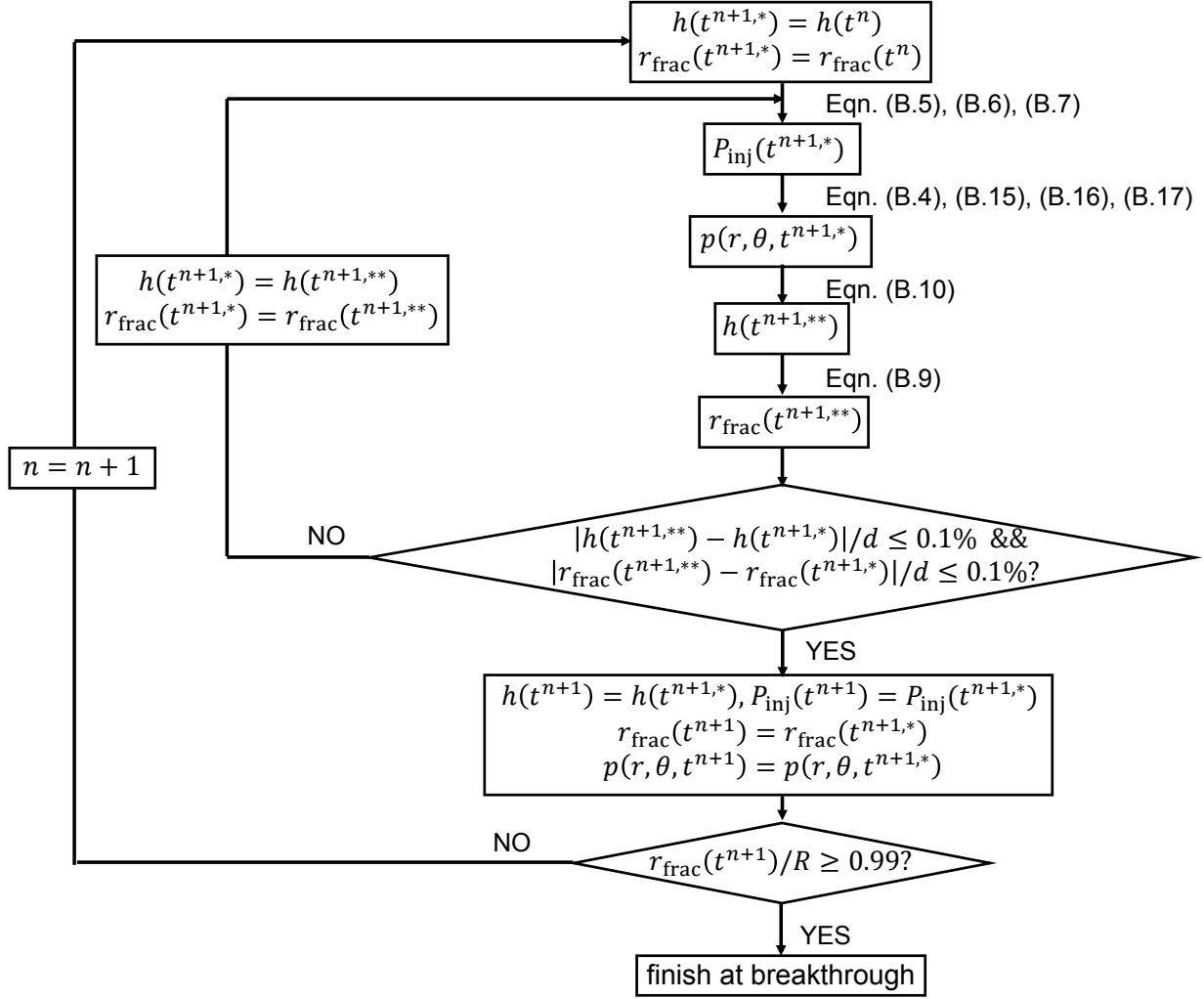


FIG. 9. Numerical implementation scheme for the mathematical model. The fluid pressure is fully coupled with granular mechanics by solving the unknown variables,  $h(t)$  and  $r_{\text{frac}}(t)$ , iteratively until convergence at each time step.